Constraints on dark matter annihilation and decay from the isotropic gamma-ray background *

Wei Liu(刘伟)[1)] Xiao-Jun Bi(毕效军)[2)] Su-Jie Lin(林苏杰) Peng-Fei Yin(殷鹏飞)

Key Laboratory of Particle Astrophysics, Institute of High Energy Physics, Chinese Academy of Sciences, Beijing 100049, China

Abstract: We study the constraints on dark matter (DM) annihilation/decay from the Fermi-LAT Isotropic Gamma-Ray Background (IGRB) observation. We consider the contributions from both extragalactic and galactic DM components. For DM annihilation, the evolution of extragalactic DM halos is taken into account. We find that the IGRB annihilation constraints under some DM subhalo models can be comparable to those derived from the observations of dwarf spheroidal galaxies and CMB. We also use the IGRB results to constrain the parameter regions accounting for the latest AMS-02 electron-positron anomaly. We find that the majority of DM annihilation/decay channels are strongly disfavored by the latest Fermi-LAT IGRB observation; only DM decays to $\mu^+\mu^-$ and 4μ channels may be valid.

Keywords: dark matter theory, gamma-ray theory, dark matter simulations, gamma-rays: diffuse background

PACS: 95.35.+d, 95.85.Pw, 98.35.Gi, 98.70.Rz **DOI:** 10.1088/1674-1137/41/4/045104

1 Introduction

Numerous observations from astrophysics and cosmology have confirmed that dark matter (DM) constitutes about 84% of the total matter in the universe [1]. Despite its acknowledged existence, we still have a poor understanding of its microscopic properties. In many new physics models, weakly interacting massive particles (WIMPs) are well-motivated DM candidates. They are expected to either self-annihilate or decay into Standard Model particles, such as neutrinos, antiprotons, electrons/positrons, photons and so on. One kind of method for DM identification, namely indirect DM detection, is to search for such signals from DM annihilation or decay. Of particular interest are gamma-ray observations with high sensitivity. Since the propagation process is simple and the energy loss is small, photons are very powerful probes to reveal DM properties.

Recently, the Fermi-LAT collaboration reported their 4-year measurement of the diffuse isotropic gamma-ray background (IGRB) at high latitudes with $|b| > 10^\circ$ [14]. Compared with the previous measurements [12, 13], the new Fermi-LAT data further extend to a higher energy range, from 0.1 GeV to 820 GeV, nearly four decades. Especially, above 300 GeV, a significant high energy cutoff has been discovered. The whole spectrum can be well described by a single power-law plus an exponential cutoff with the index $\gamma \sim 2.32\pm0.02$ and $E_{\rm cut} \sim 279\pm52$ GeV. The dominant component of the IGRB is believed to originate from extragalactic astrophysical sources, most of which are too faint or too diffuse to be resolved, such as blazars, mis-aligned active galactic nuclei and star-forming galaxies and so on. Some galactic sources, such as millisecond pulsars, can also contribute to the IGRB [43]. However, since the predicted intensity from astrophysical sources is highly model dependent, there still exists a possible contribution from DM annihilation or decay in the IGRB. Thus the IGRB is often considered to be a powerful probe to search for DM signals, and has been used to set upper limits on the DM annihilation cross section or decay lifetime in several studies [16–34, 83–85].

Another hot issue which has received considerable attention in DM studies is the excess in the cosmic ray electron-positron measurement, reported in recent years by several experiments such as PAMELA [3], ATIC [5] and Fermi [8]. Most recently, the AMS-02 results [9, 10] have confirmed such an excess from $\sim 0.5-500$ GeV with a high precision. This anomaly can be explained by DM with a large annihilation cross section to charged leptons, which is several orders of magnitudes higher than the thermal freeze-out value, i.e. 3×10^{-26} cm$^3\cdot$s^{-1}. Such DM

Received 22 July 2016, Revised 23 November 2016

∗ Supported by National Natural Science Foundation of China (11475189, 11475191, 11135009), 973 Program of China (2013CB837000), Strategic Priority Research Program "The Emergence of Cosmological Structures" of the Chinese Academy of Sciences (XDB09000000)

1) E-mail: liuwei@ihep.ac.cn

2) E-mail: bixj@ihep.ac.cn

©2017 Chinese Physical Society and the Institute of High Energy Physics of the Chinese Academy of Sciences and the Institute of Modern Physics of the Chinese Academy of Sciences and IOP Publishing Ltd

particles would also inevitably induce significant gamma-ray signals by cascade decays, internal bremsstrahlung, final state radiation (FSR), and the inverse Compton scattering (ICS) of electrons to background radiation field. Therefore, the IGRB is naturally summoned as a powerful tool to constrain DM explanations of the positron excess.

In this work, we study the constraints on the DM annihilation cross section and decay lifetime by using the latest Fermi-LAT IGRB results, and compare these limits with the DM parameter space which can explain the latest AMS-02 electron-positron observation. Compared with previous works, we have made the following improvements:

1) Both extragalactic and galactic contributions of DM annihilation/decay are reckoned. The steady-state spatial distribution of electrons and corresponding ICS gamma-rays in the Galaxy are computed by GALPROP[1)] [81, 82], which gives comprehensive consideration of the transport equation and the background radiation field.

2) Three kinds of limits, namely conservative, background-fixed, and background-relaxed, are adopted and compared with each other. The goodness of the bound depends on the limit method. Especially, we show that the shape of bound curves could vary with constraint methods.

3) New cosmic-ray data have been extensively applied. We consider recent AMS-02 proton [2], B/C [86] and electron-positron data [9, 10]. They are used to constrain transport parameters in the Galaxy [76, 77], and obtain the updated DM parameter space favored by the cosmic-ray positron anomaly.

The paper is organized as follows. In Section 2, we give a comprehensive introduction to the gamma-ray flux from DM annihilation (or decay). For extragalactic DM annihilation, the dominant theoretical uncertainties arise from the unclear clustering history and properties of small DM halos. We consider these uncertainties under different assumptions about minimum DM halos. In Section 3, we discuss the limit approach to DM annihilation (or decay) and give our analysis of the results. We derive the constraints under some different concentration models in DM annihilation. But for decaying DM, due to there being none of the above uncertainties, the constraints are quite confirmative. We also use GALPROP to calculate the propagation of the DM induced electrons and positrons, and obtain the parameter space accommodating the AMS-02 results. We compare this parameter space with the IGRB constraints. Finally, a summary is given in Section 4.

2 Diffuse gamma-rays from dark matter annihilation/decay

Both extragalactic and galactic DM can produce high energy photons. The gamma-ray flux induced by extragalactic DM depends on the history of DM clustering and is essentially isotropic. On the other hand, the spatial distribution of the galactic gamma-ray signal is apparently anisotropic due to our special position in the Galaxy. Even after rigorously subtracting the anisotropic component of galactic gamma-rays, there would still exist a residual isotropic component in the IGRB, which is equal to the signal from the direction opposite the galactic center. Thus both extragalactic and galactic DM would contribute to the IGRB signal, and the expected DM-induced IGRB flux can be written as [22, 25, 26]

$$\Phi^{\rm DM}=\Phi^{\rm DM}_{\rm EG}+\Phi^{\rm DM}_{\rm G}\Big|_{\rm anti\text{-}GC}. \tag{1}$$

2.1 Gamma-rays from cosmological dark matter evolution

The total gamma-ray flux emitted from the extragalactic annihilating DM at different redshifts is given by [16, 21, 26],

$$\Phi^{\rm anni}_{\rm EG}(E,z)=\frac{c(1+z)^2}{4\pi}\frac{\Omega^2_\chi\rho^2_{\rm c}\langle\sigma v\rangle}{2m^2_\chi}\int_z^\infty {\rm d}z'\frac{(1+z')^3[\Delta^2(z')+1]}{H(z')}\frac{{\rm d}N}{{\rm d}E'}\exp\left[-\tau(z;z',E')\right], \tag{2}$$

where m_χ is the mass of the DM particle, and $\langle\sigma v\rangle$ is the corresponding thermal averaged annihilation cross section. $H(z)=H_0\sqrt{(\Omega_\chi+\Omega_{\rm b})(1+z)^3+\Omega_\Lambda}$ and $\rho_{\rm c}=3H_0^2/8\pi G$ are the Hubble parameter at redshift z and the current critical density of the Universe, respectively. For the latest cosmological parameters Ω_χ, $\Omega_{\rm b}$, Ω_Λ and h, we refer to the values from Ref. [50]. $\Delta^2(z)$ denotes the enhancement of DM annihilation, and will be introduced in greater detail in the next subsection. In Eq. (2), z and z' are redshifts at which photons are observed and emitted respectively. ${\rm d}N/{\rm d}E'$ indicates the initial gamma-ray spectrum per DM pair annihilation, and $E'\equiv E(1+z')/(1+z)$ is the photon energy at redshift of emission z'. The prompt photons from DM annihilation are produced by final-state radiation or cascade decays of the annihilation products. In this work, the injected energy spectrum of prompt photons is generated by PPPC4DMID [15].

1) http://galprop.stanford.edu

The photons can also come from the ICS by DM-induced electrons and positrons off the interstellar radiation field, such as the cosmic microwave background (CMB), infrared photons and starlight. The gamma-ray flux from the ICS process is given by

$$\left.\frac{\mathrm{d}N}{\mathrm{d}E}\right|_{\rm IC} = c\int \mathrm{d}\epsilon\, n(\epsilon)\int \mathrm{d}E_{\rm e}\frac{\mathrm{d}n}{\mathrm{d}E_{\rm e}}\times F_{\rm KN}(\epsilon,E_{\rm e},E), \quad (3)$$

where $n(\epsilon)$ is the number density distribution of the background radiation as a function of energy ϵ at redshift z. For the cosmological ICS process, we only take into account the CMB photons. $\mathrm{d}n/\mathrm{d}E_{\rm e}$ is the energy spectrum of electrons. In this work, we adopt the assumption that electrons quickly lose their energy and the resulting distribution of electrons reaches equilibrium [18, 21]. Hence the spectrum is evaluated by equating the injected rate of DM electrons with the corresponding energy loss rate, which can be written as

$$\frac{\mathrm{d}n}{\mathrm{d}E_{\rm e}} = \frac{1}{b(E_{\rm e},z)}\int_{E_{\rm e}}^{m_\chi}\mathrm{d}E'_{\rm e}\frac{\mathrm{d}N_{\rm e}}{\mathrm{d}E'_{\rm e}}. \quad (4)$$

with the energy loss rate $b(E_{\rm e},z)\approx 2.67\times10^{-17}(1+z)^4(E_{\rm e}/\mathrm{GeV})^2$ GeV·s^{-1}. The differential Klein-Nishina cross section $F_{\rm KN}(\epsilon,E_{\rm e},E)$ is adopted as the following form [74, 75]

$$F_{\rm KN}(\epsilon,E_{\rm e},E) = \frac{3\sigma_{\rm T}}{4\gamma^2\epsilon}\Bigg[2q\ln q+(1+2q)(1-q) + \frac{(\Gamma q)^2(1-q)}{2(1+\Gamma q)}\Bigg], \quad (5)$$

where σ_T is the Thomson cross section, γ is the Lorentz factor of electron, $\Gamma=4\epsilon\gamma/m_{\rm e}$, and $q=E/\Gamma(E_{\rm e}-E)$. On a separate note, when $q<1/4\gamma^2$ or $q>1$, $F_{\rm KN}(\epsilon,E_{\rm e},E)=0$.

2.2 Clumpiness factor of dark matter annihilation

As the annihilation rate is proportional to the square of DM particle number density, the annihilation signal would be significantly enhanced in clumpy halos. The enhancement factor $\Delta^2(z)$ can be defined as summing up the contributions of all the halos with different masses formed in the history of Universe

$$\Delta^2(z) = \frac{\Delta_{\rm vir}(z)}{3\rho_\chi}\int \mathrm{d}M_{\rm vir}M_{\rm vir}\frac{\mathrm{d}n(z)}{\mathrm{d}M_{\rm vir}}\frac{\int\tilde{\rho}^2(x)x^2\mathrm{d}x}{\left(\int\tilde{\rho}(x)x^2\mathrm{d}x\right)^2}x_{\rm max}^3, \quad (6)$$

where $M_{\rm vir}$ is the virial mass of the DM halo, $\mathrm{d}n(z)/\mathrm{d}M_{\rm vir}$ is the halo mass function (see Appendix A), and $\tilde{\rho}$ is defined to describe the inner density profile of a single DM halo. Due to the self-similarity in halo formation, all halos share a common profile. Here we adopt the well-known NFW profile [46]

$$\tilde{\rho}(x) = \frac{\rho}{\rho_{\rm s}} = \frac{1}{x(1+x)^2} \quad (7)$$

with $x\equiv r/r_{\rm s}$. The scale radius $r_{\rm s}$ is related to the virial radius $r_{\rm vir}$ through

$$r_{\rm s} = \frac{r_{\rm vir}}{c_{\rm vir}}. \quad (8)$$

The virial radius $r_{\rm vir}$ can be directly derived from the virial mass $M_{\rm vir}$ by

$$r_{\rm vir} = \left(\frac{3M_{\rm vir}}{4\pi\Delta_{\rm vir}(z)\rho_\chi(z)}\right)^{1/3}, \quad (9)$$

where $\rho_\chi(z)=\rho_\chi(1+z)^3$ is the mean DM density at redshift z. The virial overdensity $\Delta_{\rm vir}(z)$ is taken to be [45]

$$\Delta_{\rm vir}(z) = (18\pi^2+82y-39y^2)/(1+y), \quad (10)$$

with $y=\Omega_m(z)-1$ and $\Omega_m(z)=\Omega_m(1+z)^3/(\Omega_m(1+z)^3+\Omega_\Lambda)$.

In Eq. (8), the concentration parameter $c_{\rm vir}$ is a function of the virial mass $M_{\rm vir}$ and redshift z. The value of $c_{\rm vir}$ is usually obtained from N-body simulation. However, halos with low masses are beyond the power of even state-of-the-art resolution. Thus their $c_{\rm vir}$ is roughly evaluated by extrapolation according to the fitting formula within the reach of simulations. The DM-induced gamma-ray flux can be enhanced by higher concentration as a result of the larger annihilation rate. In the cold dark matter (CDM) scenario, the structures are organized in 'bottom-up' fashion, i.e. smaller structures are formed earlier than larger ones. Since massive halos assemble later and experience recent major mergers, they typically hold lower concentrations compared with those growing quiescently and with smaller mass. This means that the concentration varies inversely with the halo mass [51]. Thus, the gamma-ray intensity is sensitive to the lower halo mass cut-off and the slope of the concentration model. Here we consider two concentration models: one is an analytical model developed in Ref.[47] (B01), and the other is a direct extrapolation of the fitting results from the simulation [49] (M08). In both the above models, we assume the linear redshift evolution of the concentration parameter, i.e. $c_{\rm vir}(z)=c_{\rm vir}(z=0)/(1+z)$ [47].

In this section, we compute the diffuse gamma-ray contributions of four DM benchmark points listed in Table 1. These parameter points are derived from a Markov Chain Monte Carlo (MCMC) fitting [58] to the latest AMS-02 electron/positron measurements [9, 10]. We use GALPROP to deal with the transport effect, and adopt a

conventional diffusion-convection model, which is specified in Appendix C. More comprehensive discussions are available in Ref. [76]. In the left-hand panel of Figure 1, we show the extragalactic DM-induced gamma-ray spectra under two different concentration models. The dashed and dash-dotted lines represent the spectra in the B01 and M08 models, respectively. Here the minimum DM halo mass is taken to be $M_{\rm min} = 10^{-6}M_{\odot}$. Although both B01 and M08 models provide a good fit to the concentration parameters within the resolution of the N-body simulation, the different extrapolations in the low halo mass region still produce nearly one order of magnitude difference. The low mass cutoff of the DM halo is also unclear due to the limited resolution of the N-body simulation. In the right-hand panel of Fig. 1, we show the gamma-ray spectra for different assumptions of the minimum DM halo mass $M_{\rm min} = 10^{-9}$, 10^{-6}, and $10^{5}M_{\odot}$ in the B01 model. We can see that the gamma-ray intensity gradually rises with decreasing $M_{\rm min}$. In the rest of this paper, we always take the minimum halo mass to be $M_{\rm min} = 10^{-6}M_{\odot}$. Note that here the effect of extragalactic background light has been included, which will be further explained in the next subsection.

Table 1. The best-fit values of mass-cross section (decay lifetime) parameter space for the latest AMS-02 positron-electron data [9, 10]. The DM are chosen to annihilate (decay) into $\mu^+\mu^-$ and $\tau^+\tau^-$ channels.

	annihilation		decay	
channel	m_χ /GeV	$\langle\sigma v\rangle$ /(10^{-23} cm$^3\cdot$s^{-1})	m_χ /GeV	τ /(10^{26} s)
$\mu^+\mu^-$	417.44	0.30	808.63	9.13
$\tau^+\tau^-$	1007.84	2.11	1774.76	3.21

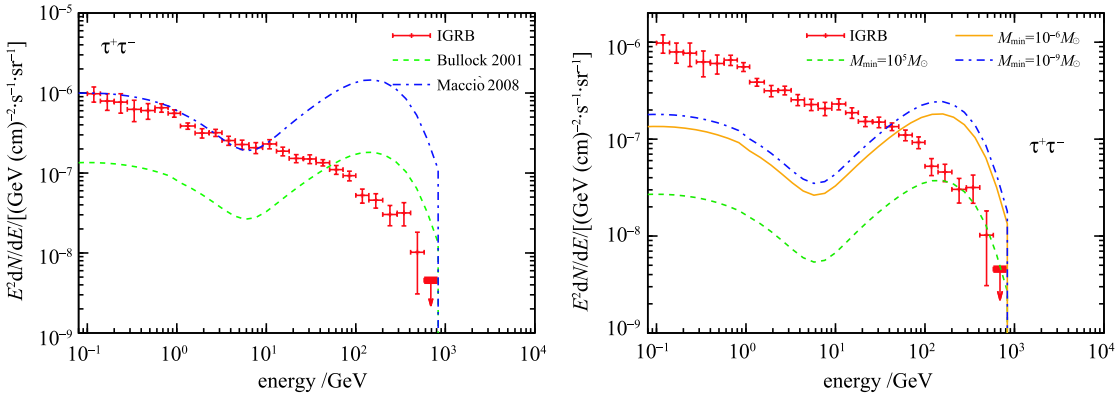

Fig. 1. (color online) Left: the extragalactic gamma-ray spectra due to different sets of the concentration parameter $c_{\rm vir}$. The annihilation channel is chosen to be $\chi\chi \to \tau^+\tau^-$. The green dashed and blue dash-dotted lines represent the spectra in the B01 [47] and M08 [49] models, respectively. Here the minimum DM halo mass is $M_{\rm min} = 10^{-6}M_{\odot}$. Right: the same gamma-ray spectra assuming different minimum DM halo masses. The blue dash-dotted, yellow solid and green dashed lines correspond to $M_{\rm min} = 10^{-9}$, 10^{-6}, $10^{5}M_{\odot}$ respectively in the B01 model.

2.3 Extragalactic background light

The factor $\exp[-\tau(z;z',E')]$ characterizes the absorption of gamma-ray photons when crossing the universe. $\tau(z;z',E')$ is the optical depth of gamma photons between observed redshift z and emission redshift z', and is obtained by the following relation:

$$\tau(z;z',E') = c\int_{z}^{z'} {\rm d}z'' \frac{\alpha(E'',z'')}{H(z'')(1+z'')}, \qquad (11)$$

where $E'' = E'(1+z'')/(1+z')$, and $\alpha(E,z)$ is the absorption coefficient. As far as we are concerned, the dominant energy loss of high energy photons is from scattering with extragalactic UV background light. In this work, we refer to the UV background model given by Ref. [54]. The UV background mainly affects the gamma-ray flux above 100 GeV, which is suppressed by roughly one order of magnitude. We also consider other energy loss processes: pair production on neutral matter ($6 < z < 1000$), pair production on fully ionized matter ($z < 6$), photon-photon scattering and photon-photon pair production with the CMB photons [15]. These interactions give a very small contribution to the attenuation of high energy gamma-ray photons.

In the left-hand panel of Fig. 2, we show the extragalactic gamma-ray spectra with and without the absorption effect of extragalactic background light (EBL). The annihilation is chosen to be the $\chi\chi \to \tau^+\tau^-$ channel. Here the concentration model is chosen to be B01. It is apparent that EBL mainly influences the high energy gamma-ray spectra, above tens of GeV. The blue dashed and purple solid lines are the galactic gamma-ray flux and the total flux with EBL, respectively.

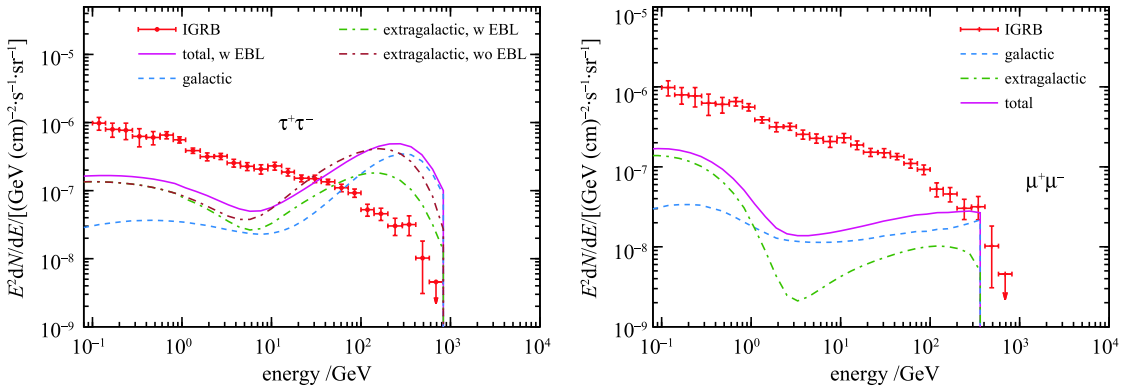

Fig. 2. (color online) Left: the influence of extragalactic background light (EBL). The green dash-dotted and brown dash-dotted lines represent the extragalactic flux with and without EBL. The blue dashed line is the galactic contribution. The purple solid line is the total flux with EBL. The annihilation channel is $\chi\chi \to \tau^+\tau^-$. Right: the galactic (blue dashed line), extragalactic (green dash-dotted line) and total (purple solid line) gamma-ray flux from $\chi\chi \to \mu^+\mu^-$ channels of DM annihilation. The DM particle cross section and mass are listed in Table 1.

2.4 Diffuse gamma-rays from galactic dark matter annihilation

The gamma-ray signal from the annihilation of galactic DM particles is obtained by the line-of-sight integral of squared DM density at an angle ψ with respect to the direction of the galactic center. The prompt radiation is given by

$$\Phi_{\rm G}^{\rm Prompt}(E,\psi) = \langle\sigma v\rangle \frac{R_\odot \rho_\odot^2}{8\pi m_\chi^2} \frac{{\rm d}N}{{\rm d}E} \times \int_{\rm l.o.s.} \left[\frac{\rho(r(x,\psi=\psi(b,\ell)))}{\rho_\odot}\right]^2 \frac{{\rm d}x}{R_\odot} . \quad (12)$$

$r(b,\ell,x) = \sqrt{R_\odot^2 - 2xR_\odot\cos(\ell)\cos(b) + x^2}$ is the distance to the galactic center, where (b,l) are galactic coordinates. Due to the finite resolution of the telescope, the gamma-rays are actually received from a finite observational solid angle. Therefore the predicated gamma-ray flux from DM annihilation should be averaged within a solid angle $\Delta\Omega$ toward an observational region

$$\bar{\Phi}_{\rm G}^{\rm Prompt}(E,\psi) = \langle\sigma v\rangle \frac{R_\odot \rho_\odot^2}{8\pi m_\chi^2} \frac{{\rm d}N}{{\rm d}E} \int_{\Delta\Omega} \frac{{\rm d}\Omega}{\Delta\Omega} \int_{\rm l.o.s.} \left[\frac{\rho(r(b,\ell,x))}{\rho_\odot}\right]^2 \frac{{\rm d}x}{R_\odot} . \quad (13)$$

We find that for the case of the anti-galactic direction, this average brings about negligible improvement. For the density distribution of the galactic DM halo, we still adopt the NFW density profile, fixing the local DM density $\rho(r=r_\odot)=0.3$ GeV/cm^3 and total DM mass within 60 kpc $M(\leqslant 60\ {\rm kpc}) = 4.7\times10^{11}\ {\rm M}_\odot$, which means $r_s = 24.42$ kpc and $\rho_s = 0.184$ GeV/cm^3 [15].

For the gamma-rays from the ICS by DM-induced high energy electrons, we need to solve the transport equation of electrons in the Galaxy. However, high energy electrons can only travel a few hundred parsecs due to the significant energy loss. Thus, the observed electrons mainly originate from nearby sources. Unlike the extragalactic ICS process, the background photons include two additional components as well as the CMB photons: infra-red light from the absorption and re-emission of starlight by galactic dust, and starlight from stars in the galactic disk. Both of these are mostly distributed in the galactic disk and are spatially dependent. Yet the usual analytical solutions of the transport equation often make a simplified assumption on the radiation field. In this work, the package GALPROP is used to numerically solve the transport and ICS processes of electrons, in which the spatial distribution of background radiations has been included. The spectra of initial electrons injected by DM are still evaluated by PPPC4DMID [15]. The transport parameters are consistent with those used to explain the latest AMS-02 results [76].

For the galactic DM annihilation, we still consider the boost factor due to DM substructures. Many analytic arguments and numerical simulations have confirmed the presence of substructure in the galactic DM halo [71–73]. We refer to the analytic substructure model developed by [67, 68], which is introduced in Appendix B. This method can extend to mass scales which are too small to be resolved by numerical simulations.

In Fig. 2, we compare the galactic gamma-ray flux with the extragalactic contribution. The annihilation channels are respectively $\chi\chi \to \tau^+\tau^-$ and $\chi\chi \to \mu^+\mu^-$. For the $\tau^+\tau^-$ channel, prompt radiation makes the stronger contribution. The galactic contribution exceeds the extragalactic one at higher energy, about hundreds of GeV. But for the $\mu^+\mu^-$ channel, the prompt radiation flux is significantly weaker than the ICS flux, thus the galactic flux holds a dominant position at lower energy,

about several GeV.

2.5 Gamma-rays from DM decay

Compared with annihilating DM, the gamma-ray intensity from decaying DM is only proportional to the cosmological DM density ρ_χ. Thus it does not suffer from enormous uncertainties, such as the density profile of the DM halo, the history of structure formation, concentration parameter, halo mass function and so on. In this case, the resulting predictions should be relatively more solid. The accumulated DM-induced gamma-ray flux during the evolution of universe is given by [22, 23, 25]

$$\Phi_{\rm EG}^{\rm dec} = \frac{c}{4\pi}\frac{\Omega_\chi \rho_{\rm c}}{m_\chi \tau_{\rm dec}} \int \frac{{\rm d}z'}{H(z')}\frac{{\rm d}N}{{\rm d}E'}\exp[-\tau(z;z',E')], \quad (14)$$

with $\tau_{\rm dec}$ the decay lifetime of the DM particle. For the prompt contribution from galactic DM decay, we just need to make the following substitution in Eq. (13):

$$\frac{\rho^2\langle\sigma v\rangle}{2m_\chi^2} \to \frac{\rho}{m_\chi \tau} \ . \quad (15)$$

The spatial distribution and energy spectrum of electrons from galactic DM decay, and the ICS contribution to photons, are also evaluated by GALPROP.

The left- and right-hand panels of Fig. 3 show the gamma-ray spectra for the $\chi \to \tau^+\tau^-$ and $\chi \to \mu^+\mu^-$ channels, respectively. Both the galactic (short dashed) and extragalactic (dash-dotted) contributions are also shown.

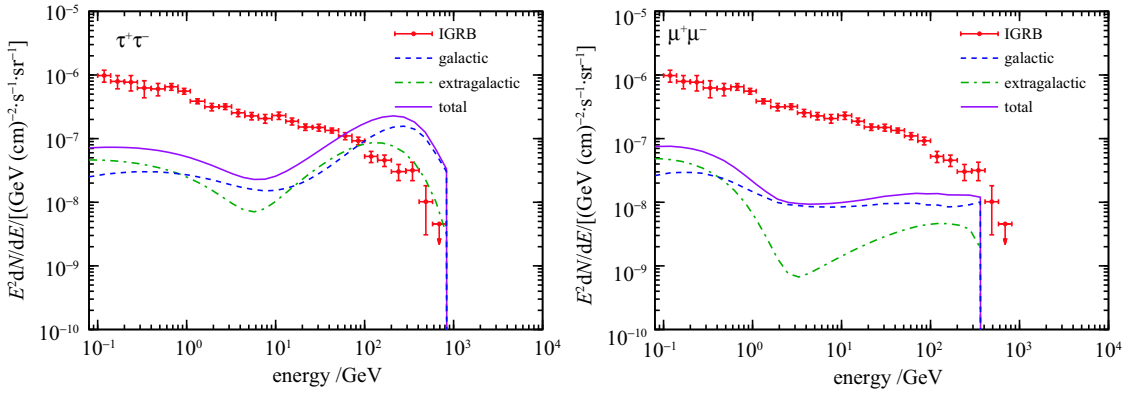

Fig. 3. (color online) The galactic (blue dashed line), extragalactic (green dash-dotted line) and total (purple solid line) gamma-ray flux from different DM decay channels. The left is the $\chi \to \tau^+\tau^-$ channel, and the right is the $\chi \to \mu^+\mu^-$ channel. The cross section and mass are listed in Table 1.

3 Constraints on DM annihilation/decay

3.1 Methods

The main component of the observed IGRB is believed to originate from unresolved astrophysical sources. In principle, the DM-induced signals can be obtained by subtracting all the astrophysical contributions from the Fermi-LAT data. The possible dominant candidates include blazars (including Flat Spectrum Radio Quasars and BL Lacertae) [37, 39, 40], star-forming galaxies [35, 36], and misaligned AGN [41, 42]. In recent years, some authors have performed analysis by fitting the IGRB data with the astrophysical contributions along with their predicted theoretical uncertainties, and then setting upper limits on the DM contribution [27–29, 31, 32]. Some studies have claimed that the extragalactic gamma-ray background above 50 GeV can be principally attributed to blazars [44]. However, the precise contributions of different populations are model dependent and remain unclear. In this work, we do not focus on the predictions and uncertainties of signatures from astrophysical sources, while adopting some model-independent methods to set constraints on DM annihilation/decay.

Conservative limits: As a first analysis, we require that the DM contributions alone should not exceed the observed IGRB spectra. The derived constraint is usually regarded as the most conservative one. The χ^2 can be defined in energy bins where the DM signal exceeds the IGRB intensity, i.e.

$$\chi^2_{\rm cons} = \sum_{i\in\{i|\phi_i^{\rm DM}>D_i^{\rm max}\}} \frac{[D_i^{\rm max}-\phi_i^{\rm DM}]^2}{\sigma_i^2}. \quad (16)$$

$\phi_i^{\rm DM}$ is the DM-induced gamma-ray flux in the i-th energy bin as a function of $\langle\sigma v\rangle$ or $t_{\rm dec}$. We adopt the IGRB background based on the galactic emission model A in Ref. [14]. However, to avoid the influence of the foreground diffuse emission model on the DM constraints, the foreground uncertainties $\sigma_i^{\rm fg}$ are incorporated into the IGRB data points D_i. All these new data points are

called $D_i^{\max}$. σ_i are kept unchanged. Our method is consistent with Ref. [30]. The corresponding 3σ DM limits are achieved when $\chi^2_{\rm cons}=9$.

Background fixed: We assume a universal function to represent the total energy spectra from astrophysical sources. Its form is taken as a single power-law with an exponential cutoff at high energy

$$\phi^{\rm bg}=I_0\left(\frac{E}{100\ {\rm MeV}}\right)^{\gamma}\exp\left(-\frac{E}{E_{\rm c}}\right), \tag{17}$$

where I_0, γ, and $E_{\rm c}$ are kept to be the best-fit values to the IGRB spectra under foreground model A [14]. The DM-induced photon flux is assumed to be superimposed on the background flux. This method was widely employed in past studies [20, 25, 30]. The χ^2 is evaluated over all the energy bins:

$$\chi^2_{\rm sens}=\sum_i\frac{[D_i-\phi_i^{\rm bg}(I_0,\gamma,E_{\rm c})-\phi_i^{\rm DM}]^2}{\sigma_i^2}. \tag{18}$$

The 3σ limits are reached when the DM signal component forces the χ^2 to rise by more than 9 with respect to the best-fit χ^2 without DM signal.

Background relaxed: In this case, the astrophysical background is also assumed to be a single power-law plus an exponential cutoff, whereas I_0, γ, and $E_{\rm c}$ are treated as free parameters as well as m_χ and $\langle\sigma v\rangle$(or $t_{\rm dec}$). For given m_χ and $\langle\sigma v\rangle$(or $t_{\rm dec}$), we can obtain a minimal χ^2 via a global fitting to the IGRB data. The upper limit on $\langle\sigma v\rangle$ (or lower limit on $t_{\rm dec}$) can be obtained when the corresponding χ^2 deviates from the minimal value $\chi^2_{\rm min}$ by a particular value, which is 9 here. Here, GNU Scientific Library (GSL)[1)] is used to perform the nonlinear least-squares fit.

3.2 Results

In Fig. 4, we show the IGRB limits on the DM annihilation cross section for nine different channels: e^+e^-, $\mu^+\mu^-$, $\tau^+\tau^-$, W^+W^-, $u\bar{u}$, $b\bar{b}$, 4μ, 4τ and $4\pi^0$. Here we adopt the concentration model B01 [47] and set $M_{\rm min}$ to be $10^{-6}M_\odot$. The three types of curve represent the constraints of conservative (blue), background-fixed (red) and background-relaxed (green) methods, respectively. Compared with the conservative limits, the background-fixed limits on the DM annihilation cross section can be improved by about one order of magnitude in the mass region of $\sim\mathcal{O}(10^2)$ GeV. The background-relaxed limits are always sandwiched between the conservative and background-fixed limits. For low DM masses, they are as stringent as the background-fixed limits. For the $\tau^+\tau^-$, $u\bar{u}$, 4τ and $4\pi^0$ channels, these limits could even reach the thermal cross section $\langle\sigma v\rangle\sim3\times10^{-26}$ cm$^3\cdot$s^{-1} at the mass region of $\sim\mathcal{O}(10)$ GeV. When the DM mass increases, all the constraints become loose and their distinctions decrease. The background-relaxed limits tend to the conservative limits at the DM mass region of $\mathcal{O}(10)$ TeV.

For comparison, the constraints from the latest Fermi-LAT observations of dwarf galaxies [61] and Planck's CMB measurements [1] are also shown in Fig. 4. For the hadronic channels, the IGRB limits are always weaker than those of dwarf galaxies at low DM mass region. However, the IGRB observations could set stringent bounds for heavy DM particles annihilating to leptons as a result of large contributions from ICS processes. This is particularly clear for the e^+e^- channel, as shown in Fig. 4. Compared with CMB limits, except for the e^+e^- and $4\pi^0$ channels, the IGRB constraints are always weaker than the updated CMB constraints. At low DM mass, the constraints from IGRB are significantly stronger for the $4\pi^0$ channel, while beyond 1000 GeV the constraints lose their strength quickly. Different from the $4\pi^0$ channel, the background-fixed constraints on the e^+e^- channel are slightly stronger at higher mass.

In Fig. 4, we also show the parameter regions accounting for the cosmic-ray electron-positron anomaly renewed by the AMS-02 collaboration. The favored DM annihilation cross section and DM mass are derived from a global MCMC fit to the AMS02 data, see Appendix C. Here we do not consider the e^+e^- final states, since the corresponding sharp electron-positron spectra cannot fit the current AMS-02 data. The same applies to the $4\pi^0$ channel, which does not generate electrons and positrons. As shown in Fig. 4, the available regions for leptonic channels are much smaller than those for hadronic channels and the DM masses required by the leptonic channels are also smaller than those for hadronic channels. We can see that almost all the channels have been excluded by the background-fixed IGRB limits. The parameter region for the $\mu^+\mu^-$ channel, although it remains valid by both conservative and background-relaxed limits, has been rejected by the updated limits from dwarf galaxies and CMB. Besides, despite the IGRB being unable to constrain the 4μ channel, it has been excluded by the CMB observation.

In Fig. 5 we show the IGRB limits on the DM annihilation cross section for the concentration model M08 [49]. All the limits are improved by almost one order of magnitude. This can be understood by the energy spectra shown in Fig. 1. At low DM masses, the IGRB limits are already comparable to those from dwarf galaxies [61], which tend to 10^{27} cm$^{-3}\cdot$s^{-1}. In this case, even the parameter space favored by the positron anomaly in $\mu^+\mu^-$ channel has been excluded readily by the conservative IGRB limit. Except for the $\mu^+\mu^-$, 4μ and $4\pi^0$ chan-

1) http://www.gnu.org/software/gsl/

nels, the background-fixed constraints are comparable or even stronger than the current CMB constraints over the whole mass range. Since the constraint curves are flatter for the $\mu^+\mu^-$ and 4μ channels, it is only comparable to the CMB limits at higher mass. For the $4\pi^0$ channel, the IGRB constraints are stronger than the CMB limit up to 5×10^5 GeV.

In Fig. 6, we present the constraints on the lifetime of decaying DM. In contrast to DM annihilation, the gamma-ray fluxes generated by decaying DM are not significantly affected by the history of the structure formation. Therefore, the constraints on the DM lifetime are more credible. The most stringent constraints come from both e^+e^- and $4\pi^0$ channels, which reach $\tau\sim10^{28}$ s respectively at $\mathcal{O}(10)$ TeV and $\mathcal{O}(1)$ TeV. For the e^+e^- channel, the main contributions are photons from ICS, while the peak of energy spectra at high energies would become significant and easily constrained by Fermi-LAT data when DM mass increases. For the $4\pi^0$ channel, the signal stems from final state radiation, whose energy range is around DM mass. In this case, the IGRB constraints are only sensitive to DM particles whose masses are less than the upper limits of the Fermi-LAT measurements. Hence, the constraints on the $4\pi^0$ channel are much weaker above 10^3 GeV, which is beyond the current Fermi-LAT observations. For the remaining channels, the limits are also stringent for low DM mass due to the contributions from cascade decay and

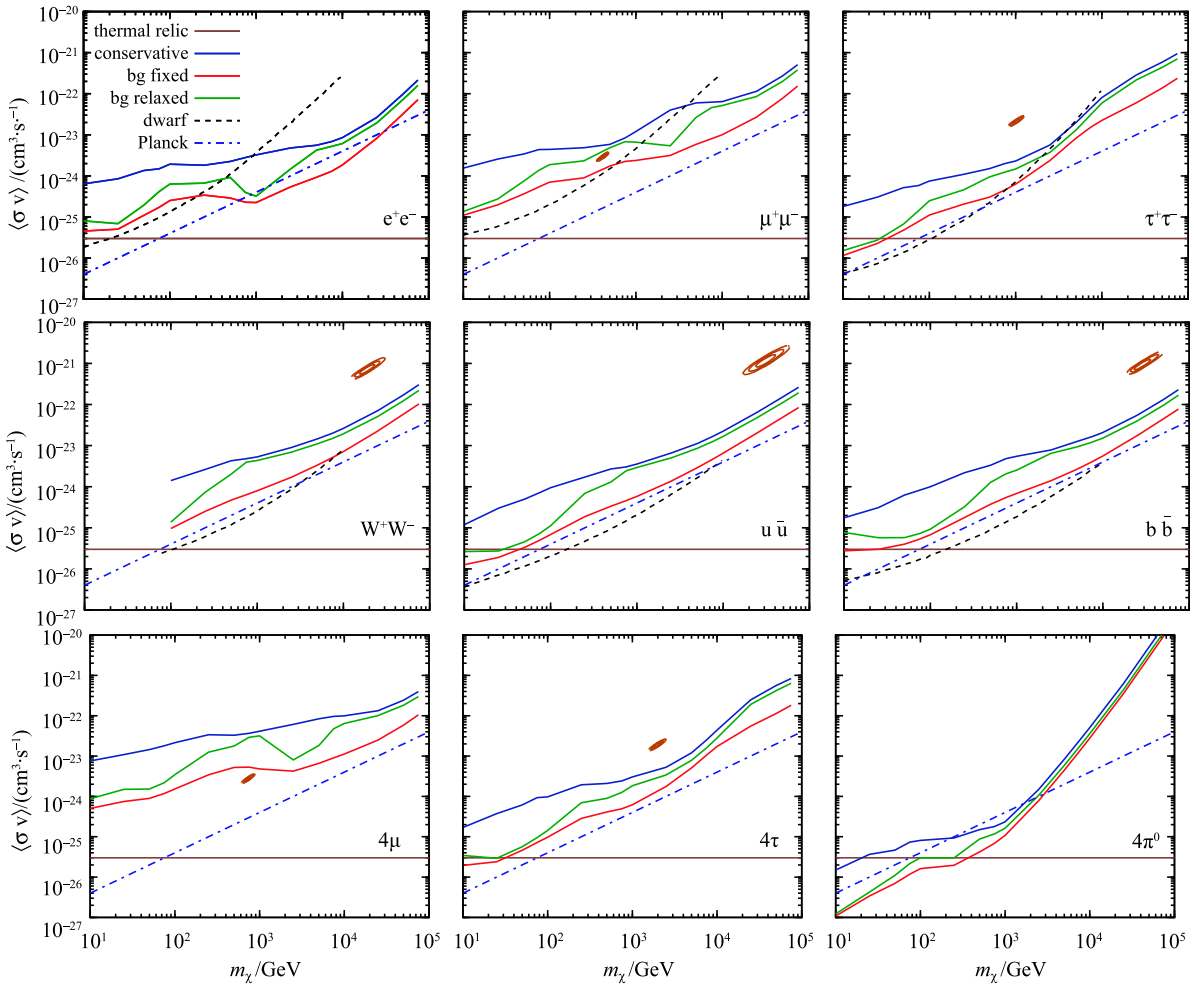

Fig. 4. (color online) The constraints on the DM annihilation cross section for nine different DM annihilation channels: e^+e^-, $\mu^+\mu^-$, $\tau^+\tau^-$, W^+W^-, $u\bar{u}$, $b\bar{b}$, 4μ, 4τ and $4\pi^0$. The concentration model B01 [47] is adopted and $M_{\rm min}=10^{-6}M_\odot$. The blue, red and green solid lines denote the conservative, background-fixed and background-relaxed limits, respectively. The brown solid line denotes the annihilation cross section for the thermal relic density $\sim3\times10^{-26}$ cm^{3}s^{-1}. Black dashed lines are the constraints from the Fermi-LAT observations of dwarf spheroidal galaxies [61], while blue dash-dotted lines are the updated CMB limits from the Planck satellite [1]. The dark orange contours correspond to the 1σ, 2σ and 3σ parameter regions accounting for the electron-positron excess observed by the AMS-02 collaboration [9, 10].

hadronization processes. The regions in parameter space favored by the positron anomaly are also manifested. All the channels are disfavored by the background-fixed limits. Only the $\mu^+\mu^-$ and 4μ channels remain allowed by the IGRB constraints.

4 Summary

We have used the latest Fermi-LAT IGRB data to set upper(lower) limits on the DM annihilation cross section(decay lifetime) for nine channels, i.e. e^+e^-, $\mu^+\mu^-$, $\tau^+\tau^-$, W^+W^-, $u\bar{u}$, $b\bar{b}$, 4μ, 4τ and $4\pi^0$. To consider the uncertainties from the multiplier of the extragalactic gamma-ray flux, the DM annihilation constraints were investigated in two competing parameterized concentration models, i.e. B01 [47] and M08 [49]. In our analysis, we derived three kinds of limits, namely conservative, background-fixed and background-relaxed limits. Compared with the conservative method, the background-fixed method can improve the constraints by about one order of magnitude at low DM masses. If a combined fit accounting for both DM-induced flux and the astrophysical background is performed, the corresponding background-relaxed limits always lie between the conservative and background-fixed limits.

For DM annihilation, we find the most stringent bounds are from $4\pi^0$ channel. In the concentration parameter model M08, the upper limit to $\langle\sigma v\rangle$ for $4\pi^0$ channel can be up to 10^{-27} cm$^3\cdot$s^{-1}. However, the constraints dramatically weaken if DM mass is heavier than $\sim\mathcal{O}(1)$ TeV, since the major contribution of gamma-rays comes from prompt radiation. The background-fixed limits for hadronic channels can be comparable with the dwarf galaxy limits. For the leptonic channels, when the DM mass is larger than $\sim\mathcal{O}(1)$ TeV, the constraints can be even stronger. This indicates that the IGRB is suitable to search for heavy DM. Compared with CMB limits, the IGRB constraints on hadronic and τ channels are comparable across the whole DM mass range. For e and μ channels, due to the flatter constraint curves, the IGRB constraints are significantly weaker than CMB constraints at lower DM mass.

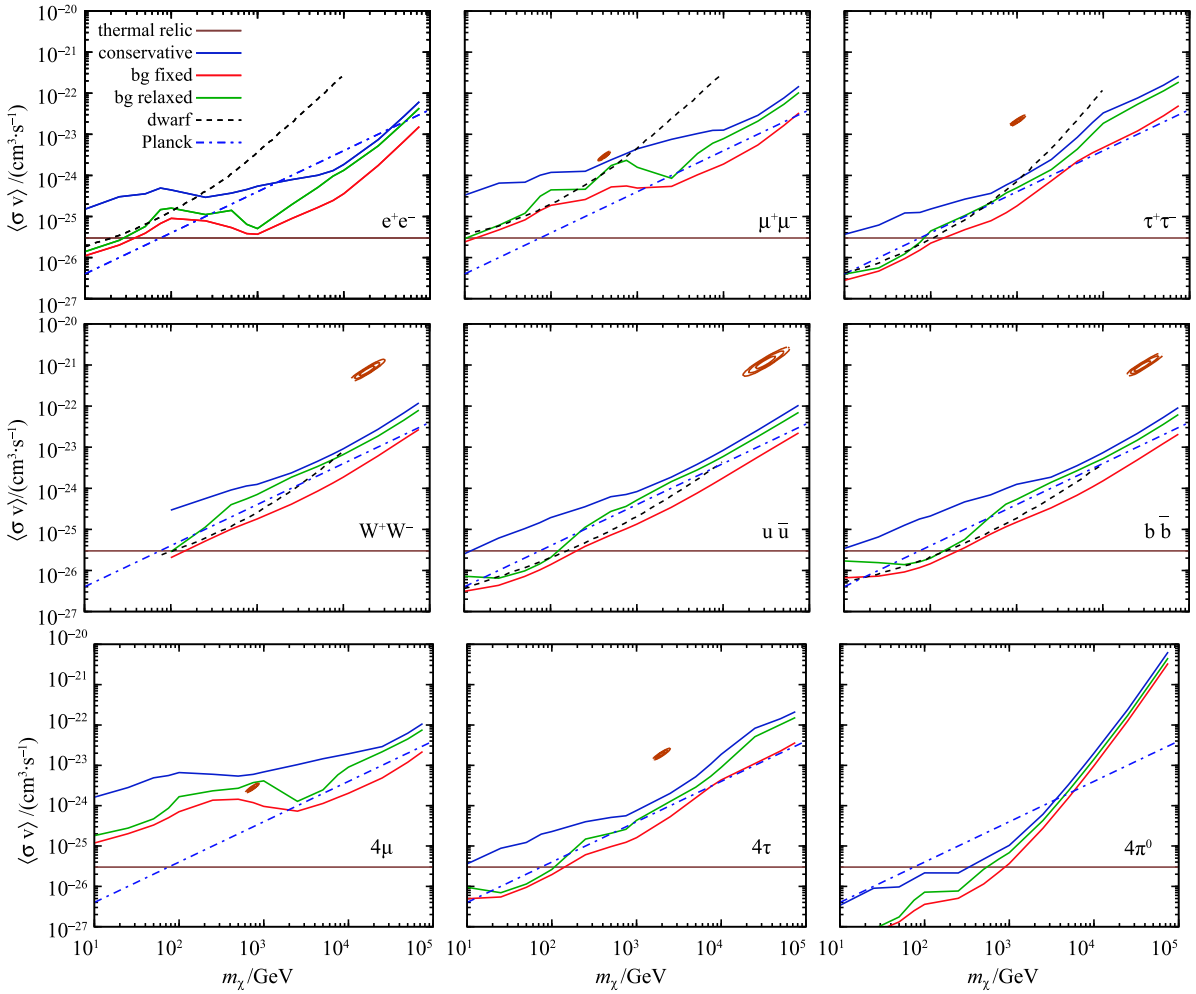

Fig. 5. (color online) The constraints on the DM annihilation cross section for nine different DM annihilation channels, where concentration model M08 [49] is adopted. The notations are the same as Fig. 4.

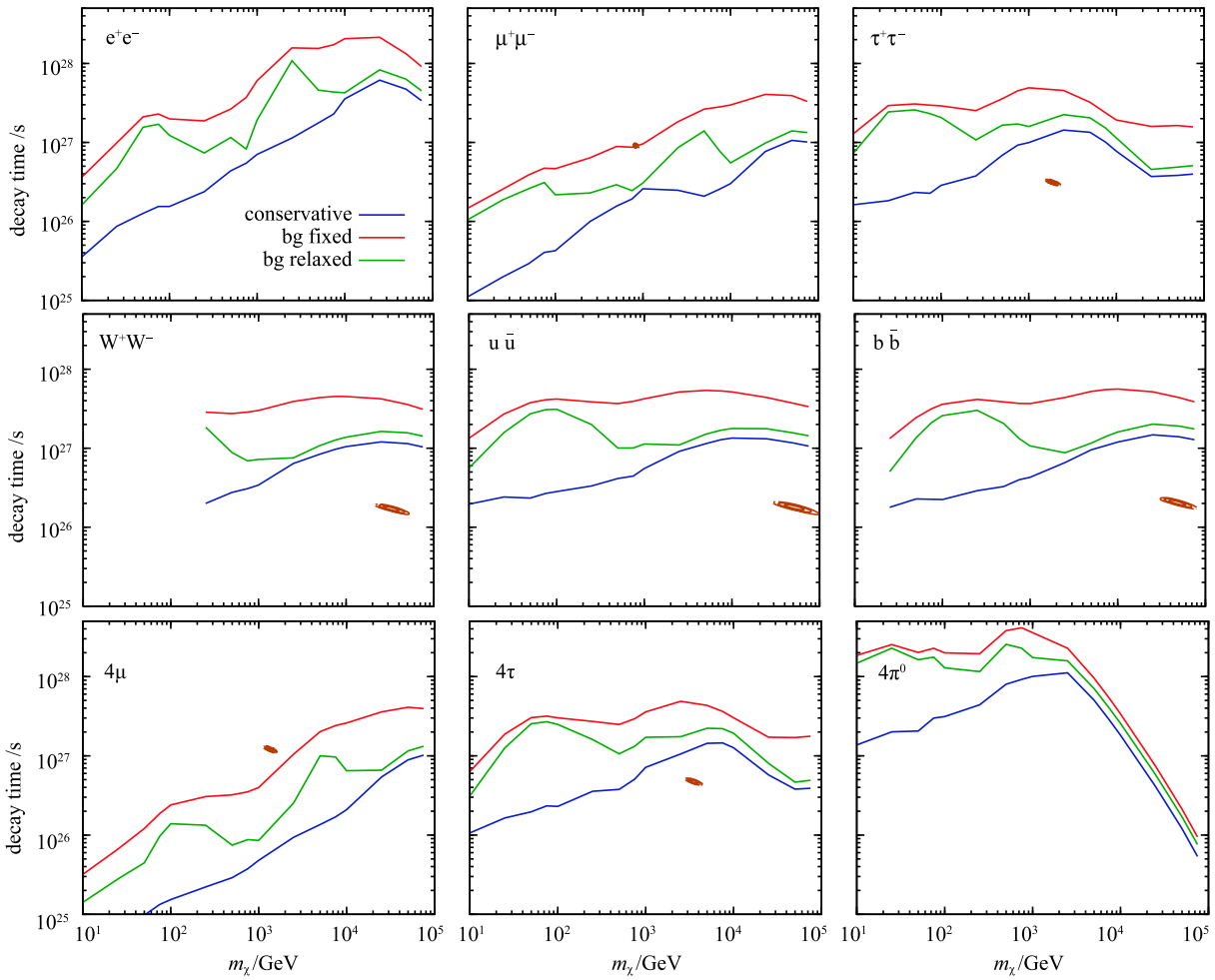

Fig. 6. (color online) The constraints of DM decay channels. The blue solid lines are the conservative limits, the red solid lines are the background-fixed limits and the green solid lines are the background-relaxed limits. The dark orange contours are the parameter space favored by the cosmic-ray electron-positron excess.

We also investigated the IGRB constraints on the parameter regions favored by the cosmic-ray electron-positron excess. We find that almost all the annihilation channels have been excluded by the background-fixed limits. Only the 4μ channel remains valid by the conservative limit in the concentration model M08. Even so, it is still excluded by update CMB limts from Planck. For decaying DM, the most stringent constraint is set for the e^+e^- and $4\pi^0$ channels, which can reach even $\tau \sim 10^{28}$ s respectively at some mass ranges. Most decay channels favored by the electron-positron anomaly have also been excluded by the conservative limits except for the $\mu^+\mu^-$ and 4μ channels, but the background-fixed limit is close to the border of the 3σ contours of the $\mu^+\mu^-$ channel. Future observations will place more stringent constraints on both channels.

W. L. thanks Qiang Yuan, Bin Yue and Dahai Yan for helpful discussions of parameter constraint, structure formation and extragalactic background light.

Appendix A

Halo mass function

The halo mass function $\mathrm{d}n(z)/\mathrm{d}M_{\rm vir}$ characterizes the comoving number density distribution of DM halos at different redshifts. It can be usually written in the following widespread formula

$$\frac{\mathrm{d}n(z)}{\mathrm{d}M_{\rm vir}} = \frac{\rho_{\rm X}}{M_{\rm vir}} \sqrt{\frac{2A^2a}{\pi}} \left[1+(a\nu^2)^{-p}\right] \exp\left(-a\nu^2/2\right) \frac{\mathrm{d}\nu}{\mathrm{d}M_{\rm vir}} \tag{A1a}$$

with $(A,a,p)=(0.322,0.707,0.3)$, i.e. the well-known Sheth-Tormen formula. $\nu=\delta_c(z)/\sigma(M_{\rm vir})$ and $\delta_c(z)=1.68[D(z=0)/D(z)]$ is the critical overdensity above which spherical collapse occurs [48]. $D(z)$ is the linear growth factor representing the growth of the density perturbation inside the horizon after matter-radiation equality era. A prevailing approximation can be found in Refs. [51, 52],

$$D(z)\simeq\frac{5\Omega_m/2}{(1+z)[\Omega_m^{4/7}-\Omega_\Lambda+(1+\Omega_m/2)(1+\Omega_\Lambda/70)]}. \quad \text{(A1b)}$$

$\sigma^2(M_{\rm vir})$ is the average variance of the density field, which is evaluated by integrating the matter power spectrum in k-space

$$\sigma^2(M_{\rm vir})=\frac{1}{2\pi^2}\int W^2(kR_{\rm M})P_\delta(k)k^2{\rm d}k, \quad \text{(A1c)}$$

where $W(x)$ is the window function. In the literature, two window functions are often used, i.e. the top-hat window function ($W(x)=3(\sin x-x\cos x)/x^3$) and the Gaussian window function ($W(x)=\exp[-x^2/2]$). In this paper, we use the former. $P_\delta(k)$ is the matter power spectrum given by

$$P_\delta(k)=A_s(k\cdot{\rm Mpc})^{n_s}T^2(k). \quad \text{(A1d)}$$

In the above equation, constant A_s is normalized by $\sigma_8\equiv\sigma(8h^{-1}{\rm Mpc})$. $T(k)$ is the linear transfer function, and here we use its well-fitted form under an adiabatic cold DM scenario with $\Omega_{b,0}\ll\Omega_{m,0}$ [51, 53]

$$T(q)=\frac{\ln(1+2.34q)}{2.34q}[1+3.89q+(16.1q)^2+(5.46q)^3+(6.71q)^4]^{-0.25}, \quad \text{(A1e)}$$

where $q=k/\Gamma(h{\rm Mpc}^{-1})$ and $\Gamma=\Omega_{\rm m,0}h\exp[-\Omega_{\rm b,0}(1+\sqrt{2h}/\Omega_{\rm m,0})]$ describes the horizon scale at $t_{\rm eq}$.

Appendix B

Dark matter subhalos in the Galaxy

When substructures are present, the DM densities with the same radius r are no longer the same. In Ref. [68], the authors defined a probability density function $P(\rho,r)$, which represents the probability at r of the density being between ρ and $\rho+{\rm d}\rho$ as $P(\rho,r)\,{\rm d}\rho$. If f_s denotes the fraction of smooth DM component, then $1-f_s$ is that of the clumped component. According to the simulation, $f_s\sim1$, so the clumpy component only occupies a tiny portion, i.e. $1-f_s\ll1$. The part with high DM density is postulated to have a power-law distribution. The probability distribution function $P(\rho,r)$ is

$$P(\rho;r)=\frac{f_s}{\sqrt{2\pi\Delta^2}}\frac{1}{\rho}\exp\left\{-\frac{1}{2\Delta^2}\left[\ln\left(\frac{\rho}{\rho_h}e^{\Delta^2/2}\right)\right]^2\right\}+(1-f_s)\frac{1+\alpha(r)}{\rho_h}\Theta(\rho-\rho_h)\left(\frac{\rho}{\rho_h}\right)^{-(2+\alpha)}. \quad \text{(B1)}$$

The first term comes from the smooth halo component, which has a log-normal distribution with the mean density ρ_h and variance Δ^2. The second term is a high-density power-law tail due to the substructure. The fraction of smooth-halo part can be well approximated by

$$f_s(r)=1-7\times10^{-3}\left(\frac{\bar\rho(r)}{\bar\rho(r=100\,{\rm kpc})}\right)^{-0.26}, \quad \text{(B2)}$$

where $\bar\rho$ is given by the probabilistic average of ρ

$$\bar\rho(r)=\int_0^{\rho_{\rm max}}\rho P(\rho)\,{\rm d}\rho=f_s\rho_h+(1-f_s)\rho_h\begin{cases}\dfrac{1+\alpha}{\alpha}\left[1-\left(\dfrac{\rho_{\rm max}}{\rho_h}\right)^{-\alpha}\right]; & \alpha\neq0,\\ \ln\dfrac{\rho_{\rm max}}{\rho_h}; & \alpha=0,\end{cases} \quad \text{(B3)}$$

where $\rho_{\rm max}=80$ GeV·cm^{-3}. The enhancement due to substructures can be attributed to a boost factor $B(r)$, i.e.

$$B(r)=\frac{\int\rho^2\,{\rm d}V}{\int[\bar\rho(r)]^2\,{\rm d}V}=\int_0^{\rho_{\rm max}}P(\rho,r)\frac{\rho^2}{[\bar\rho(r)]^2}\,{\rm d}\rho,=f_se^{\Delta^2}+(1-f_s)\frac{1+\alpha}{1-\alpha}\left[\left(\frac{\rho_{\rm max}}{\rho_h}\right)^{1-\alpha}-1\right]. \quad \text{(B4)}$$

The first term $f_se^{\Delta^2}$ corresponds to the variation in the smooth component. Since from simulations $\Delta\lesssim0.2$, it contributes to the overall boost factor by only a few percent and can be safely neglected.

Appendix C

Estimation of the dark matter parameter space favored by AMS-02 $e^\pm$ measurements

The excess of $e^\pm$ measured by AMS-02 could stem from DM. We estimated both the background flux from SNRs and excess lepton fluxes from DM annihilation/decay, and then searched for the favored parameter estimation by comparing

with the experiment results.

The $e^{\pm}$ within the halo are confined by the magnetic field surrounding the disk of the Galaxy and contribute to the flux observed at the earth. Generally, the motion of particles inside the propagation halo is described by the diffusive transport equation, i.e.

$$\frac{\partial\psi}{\partial t}=Q(\boldsymbol{x},p)+\nabla\cdot(D_{xx}\nabla\psi-\boldsymbol{V}_c\psi)+\frac{\partial}{\partial p}p^2D_{pp}\frac{\partial}{\partial p}\frac{1}{p^2}\psi - \frac{\partial}{\partial p}\left[\dot{p}\psi-\frac{p}{3}(\nabla\cdot\boldsymbol{V}_c\psi)\right]-\frac{\psi}{\tau_f}-\frac{\psi}{\tau_r}, \tag{C1}$$

with ψ is the cosmic ray density. The terms with D_{xx}, D_{pp}, $\boldsymbol{V}_c$, $\dot{p}$, τ_f and τ_r respectively describe the spatial diffusion, diffusive re-acceleration, convection, energy-loss, fragmentation and radiative decay effects. $Q(\boldsymbol{x},p)$ is the source term. The numerical simulation code GALPROP [81, 82] is used to solve Eq. (C1). In this work, the propagation parameters in the equation were set up as the DC model of Ref. [76], see Table C1. The diffusion coefficient is defined as

$$D_{xx}=D_0\left(\frac{R}{R_0}\right)^{\delta}, \tag{C2}$$

$\mathrm{d}V/\mathrm{d}z$ is the gradient of convection and L is the halo's vertical boundary. The transport paremeters well accommodate the B/C ratio and proton spectrum observed by AMS-02.

With the propagation parameters ascertained, we can then evaluate the flux of excess $e^{\pm}$ by determining the injection of excess $e^{\pm}$. Similar to the prompt photons, the injected $e^{\pm}$ from DM annihilation/decay is also evaluated by PPPC4DMID [15]. For a certain channel, the contribution of $e^{\pm}$ from DM are determined by the DM mass m_χ and average annihilation rate $\langle\sigma v\rangle$ (or lifetime τ).

Table C1. The mean values and 1σ uncertainties of the propagation parameters. δ is set to be 0 when R is below R_0.

$D_0/$ (10^{28} cm$^2\cdot$s^{-1})	$\delta/$ GV	$R_0/$ (km$\cdot$s^{-1})	$\mathrm{d}V/\mathrm{d}z/$ (km$\cdot$s$^{-1}\cdot$kpc^{-1})	$L/$ kpc
1.95 ± 0.50	0.510 ± 0.034	4.71 ± 0.8	4.2 ± 3.2	2.5 ± 0.7

To determine the flux of background $e^{\pm}$, the injection of primary cosmic ray e^- is also needed. Following Ref. [76], the injection of background e^- is assumed as a two-break power-law in order to fit AMS-02 data, i.e.

$$q_{\mathrm{i}}=N_{\mathrm{i}}\times\begin{cases}\left(\dfrac{R}{R_{\mathrm{br}}}\right)^{-\nu_1} & R\leqslant R_{\mathrm{br}}\\ \left(\dfrac{R}{R_{\mathrm{br}}}\right)^{-\nu_2} & R>R_{\mathrm{br}}\end{cases}. \tag{C3}$$

In addition, a factor c_{e^+} is introduced to indicate the uncertainty of interstellar gas density measured inside the Galaxy.

Therefore, in this work, in a single estimation, six free parameters are involved,

$$[m_\chi,\langle\sigma v\rangle/\tau,N_{e^-},\nu_1,\nu_2,c_{e^+}].$$

We performed a six dimensional MCMC scan to find the favored range for these parameters. The favored area in the m_χ—$\langle\sigma v\rangle/\tau$ plane is then obtained as a projection of the six dimension range.

References

1 P. A. R. Ade, N. Aghanim. et al (Planck Collaboration) A&A, **594**: A13 (2016)
2 C. Consolandi et al (the AMS-02 Collaboration), arXiv:1402.0467
3 O. Adriani, G. C. Barbarino, G. A. Bazilevskaya et al, Nature, **458**: 607
4 S. Torii, T. Yamagami, T. Tamura et al, arXiv:0809.0760
5 J. Chang, J. H. Adams, H. S. Ahn et al, Nature, **456**: 362 (2008)
6 F. Aharonian, A. G. Akhperjanian, U. Barres de Almeida et al, Physical Review Letters, **101**: 261104 (2008)
7 F. Aharonian, A. G. Akhperjanian, G. Anton et al, A&A, **508**: 561 (2009)
8 A. A. Abdo, M. Ackermann, M. Ajello et al, Physical Review Letters, **102**: 181101 (2009)
9 M. Aguilar, D. Aisa, A. Alvino et al, Physical Review Letters, **113**: 121102
10 L. Accardo, M. Aguilar, D. Aisa et al, Physical Review Letters, **113**: 121101
11 C. E. Fichtel, G. A. Simpson, and D. J Thompson. ApJ, **222**: 833 (1978)
12 P. Sreekumar, D. L. Bertsch, B. L. Dingus et al, ApJ, **494**: 523 (1998)
13 A. A. Abdo, M. Ackermann, M. Ajello et al, Physical Review Letters, **104**: 101101 (2010)
14 M. Ackermann, M. Ajello, A. Albert et al, ApJ, **799**: 86 (2015)
15 M. Cirelli, G. Corcella, A. Hektor et al, Phys, **3**, 051 (2011)
16 P. Ullio, L. Bergström, J. Edsjö, and C Lacey, Phys, **66**: 123502 (2002)
17 J. E. Taylor and J Silk, MNRAS, **339**: 505 (2003)
18 S. Profumo and T. E Jeltema, J. Cosmology Astropart. Phys., **7**: 020 (2009)
19 M. Kawasaki, K. Kohri, and K. Nakayama, Phys. Rev. D, **80**: 023517 (2009)
20 A. A. Abdo, M. Ackermann, M. Ajello et al, J. Cosmology Astropart. Phys., **4**: 014 (2010)
21 Q. Yuan, B. Yue, X.-J. Bi, X. Chen, and X Zhang, J. Cosmology Astropart. Phys., **10**: 023 (2010)
22 M. Cirelli, P. Panci, and P. D. Serpico, Nuclear Physics B, **840**: 284 (2010)
23 C.-R. Chen, S. K. Mandal, and F. Takahashi, J. Cosmology Astropart. Phys., **1**: 023 (2010)
24 S. Blanchet and J. Lavalle, J. Cosmology Astropart. Phys., **11**: 021 (2012)
25 M. Cirelli, E. Moulin, P. Panci, P. D. Serpico, and A. Viana, Phys. Rev. D, **86**: 083506 (2012)
26 K. N. Abazajian, S. Blanchet, and J. P Harding, Phys. Rev. D, **85**: 043509 (2012)
27 T. Bringmann, F. Calore, M. Di Mauro, and F. Donato, Phys. Rev. D, **89**: 023012
28 I. Cholis, D. Hooper, and S. D. McDermott, J. Cosmology Astropart. Phys., **2**: 014 (2014)
29 M. Ajello, D. Gasparrini, M. Sánchez-Conde et al, ApJ, **800**: L27 (2015)
30 The Fermi LAT Collaboration, J. Cosmology Astropart. Phys.,

9: 008 (2015)
31 M. Di Mauro and F. Donato, Phys. Rev. D, **91**: 123001 (2015)
32 S. Ando and K. Ishiwata, J. Cosmology Astropart. Phys., **5**: 024 (2015)
33 J.-Q. Xia, A. Cuoco, E. Branchini, and M. Viel, ApJS, **217**: 15 (2015)
34 A. Cuoco, J.-Q. Xia, M. Regis et al, ApJS, **221**: 29 (2015)
35 M. Ackermann, M. Ajello, A. Allafort et al, ApJ, **755**: 164 (2012)
36 B. C. Lacki, S. Horiuchi, and J. F. Beacom, ApJ, **786**: 40 (2014)
37 T. M. Venters and V. Pavlidou, ApJ, **737**: 80
38 D. Yan, H. Zeng, and L. Zhang, MNRAS, **422**: 1779 (2012)
39 H. Zeng, D. Yan, and L. Zhang, MNRAS, **431**: 997 (2013)
40 H. D. Zeng, D. H. Yan, Y. Q. Sun, and L. Zhang, ApJ, **749**: 151 (2012)
41 Y. Inoue, ApJ, **733**: 66 (2011)
42 M. Di Mauro, F. Calore, F. Donato, M. Ajello, and L. Latronico, ApJ, **780**: 161 (2014)
43 M. Fornasa and M. A. Sánchez-Conde, Phys. Rep., **598**: 1 (2015)
44 M. Ackermann, M. Ajello, A. Albert et al, Physical Review Letters, **116**: 151105 (2016)
45 G. L. Bryan and M. L. Norman, ApJ, **495**: 80 (1998)
46 J. F. Navarro, C. S. Frenk, and S. D. M. White, ApJ, **462**: 563 (1996)
47 J. S. Bullock, T. S. Kolatt, Y. Sigad et al, MNRAS, **321**: 559 (2001)
48 V. R. Eke, S. Cole, and C. S. Frenk, MNRAS, 282, (1996)
49 A. V. Macciò, A. A. Dutton, and F. C. van den Bosch, MNRAS, **391**: 1940 (2008)
50 K. A. Olive (Particle Data Group), Chinese Physics C, **38**: 090001 (2014)
51 H. Mo, F. C. van den Bosch, and S. White, *Galaxy Formation and Evolution* (Cambridge, UK: Cambridge University Press, 2010)
52 S. M. Carroll, W. H. Press, and E. L. Turner, ARA&A, **30**: 499 (1992)
53 J. M. Bardeen, J. R. Bond, N. Kaiser, and A. S. Szalay, ApJ, **304**: 15 (1986)
54 R. C. Gilmore, R. S. Somerville, J. R. Primack, and A. Domínguez, MNRAS, **422**: 3189 (2012)
55 R. J. Gould and G. Schréder, Physical Review Letters, **16**: 252 (1996)
56 F. W. Stecker, O. C. de Jager, and M. H. Salamon, ApJl, **390**: L49 (1992)
57 M. Ackermann, M. Ajello, A. Allafort et al, J. Cosmology Astropart. Phys., **5**: 025 (2010)
58 Q. Yuan, P.-F. Yin, X.-J. Bi, X.-M. Zhang, and S.-H. Zhu, Phys. Rev. D, **82**: 023506 (2010)
59 E. Nezri, R. White, C. Combet et al, MNRAS, **425**, 477 (2012)
60 A. Abramowski, F. Acero, F. Aharonian et al, Physical Review Letters, **106**: 161301 (2011)
61 M. Ackermann, A. Albert, B. Anderson et al, Phys. Rev. D, **89**: 042001 (2014)
62 M. Ackermann, A. Albert, B. Anderson et al, Physical Review Letters, **115**: 231301 (2015)
63 M. Boudaud, S. Aupetit, S. Caroff et al, A&A, **575**: A67 (2015)
64 X. Li, Z.-Q. Shen, B.-Q. Lu et al, Physics Letters B, **749**: 267 (2015)
65 E. Carquín, M. A. Díaz, G. A. Gómez-Vargas, B. Panes, and N. Viaux, Physics of the Dark Universe, **11**: 1 (2016)
66 T. Basak, S. Mohanty, and G. Tomar, Journal of High Energy Physics, **3**: 62 (2016)
67 M. Kamionkowski and S. M. Koushiappas, Phys. Rev. D, **77**: 103509 (2008)
68 M. Kamionkowski, S. M. Koushiappas, and M. Kuhlen, Phys. Rev. D, **81**: 043532 (2010)
69 L. J. Rosenberg and K. A. van Bibber, Phys. Rep., **325**: 1 (2000)
70 S. J. Asztalos, L. J. Rosenberg, K. van Bibber, P. Sikivie, and K. Zioutas, Annual Review of Nuclear and Particle Science, **56**: 293 (2006)
71 J. F. Navarro, C. S. Frenk, and S. D. M. White, ApJ, **490**: 493 (1997)
72 C. Giocoli, G. Tormen, R. K. Sheth, and F. C. van den Bosch, MNRAS, **404**: 502 (2010)
73 M. Maciejewski, M. Vogelsberger, S. D. M. White, and V. Springel, MNRAS, **415**: 2475 (2011)
74 G. R. Blumenthal and R. J. Gould, Reviews of Modern Physics, **42**: 237 (1970)
75 F. C. Jones, Physical Review, **167**: 1159 (1968)
76 S.-J. Lin, Q. Yuan, and X.-J. Bi, Phys. Rev. D, **91**: 063508 (2015)
77 S.-J. Lin, X.-J. Bi, P.-F. Yin, and Z.-H. Yu, arXiv:1504.07230
78 K. Hamaguchi, T. Moroi, and K. Nakayama, Physics Letters B, **747**: 523 (2015)
79 M. Ibe, S. Matsumoto, S. Shirai, and T. T. Yanagida, Phys. Rev. D, **91**: 111701 (2015)
80 C.-H. Chen, C.-W. Chiang, and T. Nomura, Physics Letters B, **747**: 495 (2015)
81 I. V. Moskalenko and A. W. Strong, ApJ, **493**: 694 (1998)
82 A. W. Strong and I. V. Moskalenko, ApJ, **509**: 212 (1998)
83 Y. Yang, L. Feng, X. Huang et al, J. Cosmology Astropart. Phys., **12**: 020 (2011)
84 K. Murase and J. F. Beacom, J. Cosmology Astropart. Phys., **10**: 043 (2012)
85 K. C. Y. Ng, R. Laha, S. Campbell et al, Phys. Rev. D, **89**, 083001 (2014)
86 AMS-02 Collaboration, http://www.ams02.org